Dalton Transactions

Accepted Manuscript

ROYAL SOCIETY OF CHEMISTRY

www.rsc.org/dalton

Cite this: DOI: 10.1039/c0xx00000x

www.rsc.org/xxxxxx

ARTICLE TYPE

Study on the thermal conversion of scheelite-type ABO_4 into perovskite-type $AB(O,N)_3$

Wenjie Li,[a] Duan Li,[b] Xin Gao,[b] Aleksander Gurlo,[c] Stefan Zander,[e] Philip Jones,[d] Alexandra Navrotsky,[d] Zhijian Shen,[b] Ralf Riedel,[a] and Emanuel Ionescu[*, a]

Received (in XXX, XXX) Xth XXXXXXXXX 20XX, Accepted Xth XXXXXXXXX 20XX

DOI: 10.1039/b000000x

Phase-pure scheelite $AMoO_4$ and AWO_4 (A=Ba, Sr, Ca) were thermally treated in ammonia atmosphere at 400 to 900 °C. $SrMoO_4$ and $SrWO_4$ were shown to convert into cubic perovskite $SrMoO_2N$ and $SrWO_{1.5}N_{1.5}$, at 700 °C and 900 °C respectively, and to form metastable intermediate phases (scheelite $SrMoO_{4-x}N_x$ and $SrWO_{4-x}N_x$), as revealed by X-ray diffraction (XRD), elemental analysis and FTIR spectroscopy. High-temperature oxide melt solution calorimetry reveals that the enthalpy of formation for $SrM(O,N)_3$ (M = Mo, W) perovskites is less negative than that of the corresponding scheelite oxides, though the conversion of the scheelite oxides into perovskite oxynitrides is thermodynamically favorable at moderate temperatures. The reaction of $BaMO_4$ with ammonia leads to the formation of rhombohedral $Ba_3M_2(O,N)_8$ and corresponding binary metal nitrides Mo_3N_2 and $W_{4.6}N_4$, Similar behavior was observed for $CaMO_4$, which converted upon ammonolysis into individual oxides and nitrides. Thus, $BaMO_4$ and $CaMO_4$ were shown to not provide access to perovskite oxynitrides. The influence of the starting scheelite oxide precursor, the structure distortion and the degree of covalency of the B-site-N bond are discussed within the context of the formability of perovskite oxynitrides.

1 INTRODUCTION

Perovskite oxynitrides $AB(O,N)_3$ are typically synthesized via ammonolysis of oxide precursors; thus they can be formally represented as nitrogen-substituted perovskite-type oxides[1, 2], which exhibit an emerging class of materials suitable for novel applications in the fields of energy conversion, storage, non-toxic pigments, dielectrics, etc. [3].

Most perovskite-type oxynitrides are synthesized via conversion of scheelite-type ABO_4 and pyrochlore-type $A_2B_2O_7$ upon thermal treatment in ammonia atmosphere. However, not all scheelite- and pyrochlore-type oxides are able to access perovskite oxynitrides. For example, pyrochlore-type $La_2Zr_2O_7$ as well as scheelite-type $EuMO_4$ (M = Nb and Ta) and $SrMoO_4$ provide access to perovskite-type $LaZrO_2N$[4] as well as $EuMO_2N$[5] and $SrMoO_2N$,[6] respectively; whereas other precursor oxides such as scheelite-type $ATaO_4$ (A = Nd, Sm, Gd, Dy) and $A_2W_2O_9$ (A = Pr, Nd, Sm, Gd, Dy) convert upon ammonolysis into pyrochlore-type $A_2Ta_2O_5N_2$,[7] and scheelite-type AWO_3N,[8] respectively.

According to our previous work, only a limited number of perovskite-type oxynitrides are formable.[9] For instance, $SrMoO_2N$, $SrWO_2N$, $CaMoO_2N$ and $CaWO_2N$ appear to be feasible; while, $BaMoO_2N$ and $BaWO_2N$ are not stable in the perovskite-type structure. Although perovskite-type $SrMo(O,N)_3$, $SrW(O,N)_3$ and $CaMo(O,N)_3$ [6, 10-14] have been reported in the literature (consistent with our prediction based on tolerance and octahedral factors)[9], details of the structure evolution of the oxides into perovskite-type oxynitrides are scarce. Furthermore, the existence of perovskite-type $BaMo(O,N)_3$ is questionable[11, 12]; whereas, perovskite-type $BaW(O,N)_3$ and $CaW(O,N)_3$ have not yet been synthesized.

2 EXPERIMENTAL METHODS

2.1 Synthesis

Scheelite-type oxide precursors (i.e., $SrMoO_4$, $SrWO_4$, $BaMoO_4$, $BaWO_4$, $CaMoO_4$ and $CaWO_4$) were synthesized via solvothermal methods. Thus, $Sr(NO_3)_2$ (Sigma-Aldrich, >99.0%), $Ba(NO_3)_2$ (Sigma-Aldrich, >99.0%) or $Ca(NO_3)_2{\cdot}4H_2O$ (Sigma-Aldrich, >99.0%), was mixed in an equimolar ratio with

Na_2MoO_4▪$4H_2O$ (Sigma-Aldrich, >99.5%) or Na_2WO_4▪$4H_2O$ (Sigma-Aldrich, >99.5%) in ethylenediamine (FLUKA, > 99.5 %) under vigorous stirring. Subsequently, the reaction mixture was transferred into an autoclave with Teflon lining and heated at 200 ^{0}C for 24 h. The resulting mixture was rinsed 5 times with deionized water and ethanol alternately. Centrifugation and drying at 60 ^{0}C overnight led to the powdered scheelite-type oxides.

The resulting oxides were ground to fine powders (grain size < 500 nm) and placed in a silica crucible. The thermal treatments were carried out in flowing ammonia at temperatures between 400 and 900 ^{0}C for 4 – 24 h. The Schlenk system used for thermal ammonolysis is specifically limited to small batch sizes (about 0.3 – 0.5 g) to maximize exposure to flowing NH_3 and thus the product homogeneity.

2.2 Sample characterization

The crystalline phase composition of the as-synthesized samples was analyzed by using powder X-ray diffraction (XRD, STOE STADI P) with Mo Kα radiation (wavelength 0.7093 Å). The oxygen and nitrogen contents of the synthesized samples were determined by hot gas extraction using a LECO TC436 analyzer. Fourier Transform Infrared (FT-IR) spectroscopy was performed on a Varian 670-IR Spectrometer. Thermogravimetric analysis (TGA 92, SETARAM) under ammonia atmosphere was done to obtain the weight change of samples. High resolution transmission electron microscope (HRTEM, JEOL JEM-2100F) was used to assess the morphology and the local crystallinity of the samples.

High temperature oxidative -solution calorimetry was used to determine the enthalpies of formation of the prepared oxynitride samples. This method is well developed[15-18] and has been applied previously to study nitrides[19-21] and oxynitrides[22-24]. Using this technique, ~ 5 mg pellets, made by pressing the powders into a die with a diameter of 1mm, were dropped from room temperature into molten sodium molybdate ($3Na_2O$▪$4MoO_3$) solvent at 701 °C in a custom made Tian-Calvet twin microcalorimeter[15, 17].

Neutron diffraction (ND) experiments were performed at the high resolution powder diffractometer for thermal neutrons (HRPT)[25] located at the Swiss Spallation Neutron Source (SINQ) of the Paul Scherrer Institute in Switzerland and the Fine Resolution Powder Diffractometer (FIREPOD, E9)[26] at the BERII of the Helmholtz-Zentrum Berlin (HZB), Germany. The measurements were performed using a neutron wavelength of λ=1.494 Å at SINQ and λ=1.308 Å at HZB. Crystallographic parameters were confirmed by the individual Rietveld refinements of the XRD and ND patterns. The peak shapes were modeled with pseudo-Voigt function for XRD and Thompson-Cox-Hastings pseudo-Voigt function[27] for ND patterns. Isotropic thermal parameters of O/N were constrained to the same value for the anions. All refinements were performed with the Fullprof software[28].

3 RESULTS AND DISCUSSION

3.1 Ammonolysis of scheelite-type oxides

$BaMoO_4$ and $BaWO_4$. The ammonolysis of the scheelite-type $BaMoO_4$ was performed at 600, 700 and 900 ^{0}C for 6 h. The sample treated at 600 ^{0}C already formed small amounts of $Ba_3Mo_2(O,N)_8$ oxynitride phase (structure identical to $Ba_3Mo_2N_6N_2$ [29, 30]), as shown in Figure S1. At 700 °C, Mo_3N_2 [31] and $BaMoO_3$ [32] were observed. Up to 900 °C, only small amounts of Mo_3N_2 were detected besides the main phase $Ba_3Mo_2(O,N)_8$. The absence of the perovskite-type $BaMo(O,N)_3$ is consistent with the experimental work of Liu et al. [12] and our previously prediction[9]. The crystallographic data and phase compositions of the samples obtained at 700 and 900 ^{0}C were analyzed by Rietveld refinement (Figure S2 a and b). The refined lattice parameter of $BaMoO_3$ was 4.0489 (6) Å, which is similar to reported values[11, 33]. No cubic perovskite $BaMo(O,N)_3$ formed. The lattice parameter of the rhombohedral $Ba_3Mo_2(O,N)_8$ were 5.9670 (3) and 21.4812 (10) Å (Table S1); these values are smaller than those of $Ba_3Mo_2O_6N_2$ (5.9706 (5) and 21.5020 (6) Å)[34] probably because of the lower nitrogen content in our as-synthesized oxynitride (however, we balanced the Equations (1) – (3) based on $Ba_3Mo_2O_6N_2$ and $Ba_3W_2O_6N_2$).

A noticeable reaction between $BaWO_4$ and NH_3 occurs at 700 ^{0}C (Figure S3). Compared to $BaMoO_4$, $BaWO_4$ seems to be rather more inert against ammonia, thus more than 50 wt% of $BaWO_4$ still remained after ammonolysis at temperatures up to 850 ^{0}C (Table S2). Hence, the ammonolysis of $BaWO_4$ at 700 and 850 °C leads to a mixture consisting of $BaWO_4$, $Ba_3W_2(O,N)_8$ and $W_{4.6}N_4$. The lattice parameters of $Ba_3W_2(O,N)_8$ and $W_{4.6}N_4$ assessed by Rietveld refinement of the XRD patterns (Figure S4) are close to those reported [34] and [29] (see also the Supporting Information, Table S2 and S4). As we recently predicted [9], the perovskite-type $BaWO_2N$ cannot be formed.

The samples obtained upon ammonolysis of $BaMoO_4$ and $BaWO_4$ were also investigated by FTIR spectroscopy; both show an absorption band around 975 cm^{-1} for oxynitride (Figure S5), which was assigned to a stretching mode (ν(M-N)) in $(WO_3N)^{3-}$ / $(MoO_3N)^{3-}$, having W^{6+} / Mo^{6+} in tetrahedral coordination, as reported by Herle et al.[30]

Thus ammonolysis of the scheelite-type oxides $BaWO_4$ and $BaMoO_4$ leads to non-perovskite oxynitrides products following the paths proposed in the equations (1)-(3):

$$10BaMoO_4 + \frac{38}{3}NH_3 \xrightarrow{700\,^\circ C} 3Ba_3Mo_2(O,N)_8 + BaMoO_3 + Mo_3N_2 + 19H_2O + \frac{14}{3}N_2 \quad (1)$$

$$9BaMoO_4 + 12NH_3 \xrightarrow{900\,^\circ C} 3Ba_3Mo_2(O,N)_8 + Mo_3N_2 + 18H_2O + 2N_2 \quad (2)$$

$$69BaWO_4 + 92NH_3 \xrightarrow{850\,^\circ C} 23Ba_3W_2(O,N)_8 + 5W_{4.6}N_4 + 138H_2O + 13N_2 \quad (3)$$

$SrMoO_4$ and $SrWO_4$. A similar ammonolysis procedure was applied to the scheelite-type $SrMoO_4$ and $SrWO_4$.

XRD measurements confirm that the ammonolysis of $SrMoO_4$ at 700 °C for 4 h leads to the formation of $SrMoO_2N$ (Figure 1). The change of O/N ratio with annealing time in $SrMoO_2N$ was shown to decrease from 2.3 upon annealing time of 4 h (empirical chemical composition of the oxynitride $SrMoO_{2.09(1)}N_{0.91(1)}$) to 1.89 after 12 h ($SrMoO_{1.96(1)}N_{1.04(1)}$) and to 1.54 after 24 h of ammonolysis ($SrMoO_{1.82(1)}N_{1.18(1)}$). However, the nitrogen incorporation seems to have limitations under the used conditions, thus nitrogen-rich compositions (e.g., $SrMoON_2$, with a O/N ratio of 0.5) are not accessible in this way.

Figure 1 XRD patterns of $SrMoO_4$ after heating at 400, 600 and 700 °C for different times under an ammonia flow in forming gas (mixture of 5 vol% H_2 and 95 vol% N_2). Arrow indicates the diffraction pattern of the oxynitride obtained upon ammonolysis of $SrMoO_3$ which was synthesized by reducing $SrMoO_4$ under ammonia flow at 700 °C.

The ammonolysis of scheelite-type $SrWO_4$ at 900 °C leads to the corresponding perovskite-type oxynitride as well (Figure 2). However, the temperature required to obtain phase-pure Sr,W-based oxynitride was higher than that used for $SrMoO_4$. The nitrogen content of the $SrW(O,N)_3$ increases slightly with the increasing temperature and holding time. Moreover, the O/N ratio in $SrW(O,N)_3$ seems to be more constant as compared to that in $SrMo(O,N)_3$ and appears independent of the annealing time. Thus, the O/N ratio decreases only slightly as the annealing time was extended from 4 h ($SrWO_{1.50(6)}N_{1.50(6)}$; O/N ratio 1.08), to 12 h ($SrWO_{1.42(2)}N_{1.58(2)}$; O/N 0.98) and 24 h ($SrWO_{1.39(2)}N_{1.61(2)}$; O/N 0.86), respectively. Interestingly, the Sr,W-based system can accommodate more nitrogen than its analogous Sr,Mo-based system. Nevertheless the O/N ratio still cannot be pushed down to 0.5.

Figure 2 XRD patterns of $SrWO_4$ after heating at 400, 600, 700 and 900 °C for different time under an ammonia flow.

$CaMoO_4$ and $CaWO_4$. The ammonolysis of $CaMoO_4$ was found to proceed in a different way, leading to the formation of CaO and various molybdenum nitrides (including Mo_2N, Mo_3N_2 and MoN, depending on the temperature, time and ammonia flow) (Figure S6) and consequently $CaMoO_4$ was not considered further as a precursor for the corresponding perovskite-type oxynitrides.

Ammonolysis of $CaWO_4$ at 900 °C for 6 h leads to complete decomposition into Ca_3WO_6 and $W_{4.6}N_4$ and no oxynitride phase was observed (Figure S6). For both $CaMoO_4$ and $CaWO_4$, the corresponding perovskite oxynitrides did not formed and thus their conversion into oxide/nitride mixture is assumed to occur as follows:

$$6CaMoO_4 + 12NH_3 \xrightarrow{700\,^\circ C} 6CaO + Mo_2N + Mo_3N_2 + MoN + 18H_2O + 4N_2 \quad [4]$$

$$6.9CaWO_4 + 9.2NH_3 \xrightarrow{900\,^\circ C} 11.5Ca_3WO_6 + W_{4.6}N_4 + 13.8H_2O + 2.6N_2 \quad [5]$$

3.2 Intermediate oxynitride phase during the conversion of $SrMoO_4$ into perovskite-type $SrMoO_2N$

An interesting phenomenon during the ammonolysis of $SrMoO_4$ at 600 °C relates to the incorporation of 2.23 wt % nitrogen without the formation of any new crystalline phase; thus, the color of the sample changed from white to light-grayish and the FTIR spectrum showed a new absorption band at 978 cm^{-1} related to $(MoO_3N)^{3-}$ units in tetrahedral coordination (Figure 3a), [30] as observed also in $Ba_3Mo_2(O,N)_8$. Tetra-coordinated Mo^{6+} in scheelite-type $SrMoO_4$ can be identified by FTIR spectroscopy via very broad band around 822 cm^{-1} representing the

antisymmetric stretching vibrations of Mo-O in $(MoO_4)^{2-}$ tetrahedral units.[35] Thus, the formation of $(MoO_3N)^{3-}$ is considered to be a result of the substitution of one oxygen with nitrogen in $(MoO_4)^{2-}$ tetrahedra. Therefore, we assume that an intermediate scheelite-type oxynitride phase $SrMoO_{4-x}N_x$ (x = 0.39 in our experiment, as obtained from elemental analysis and Rietveld refinement, Figure 4) forms at 600 °C, which subsequently rearranges into the perovskite structure while taking up more nitrogen. The absence of the absorption band of $(MoO_3N)^{3-}$ in the samples obtained upon ammonolysis at temperatures above700 °C might be related to the strong absorption of the black sample.

Figure 3 FTIR spectrum of the as-synthesized scheelite oxide (a) $SrMoO_4$, (b) $SrWO_4$ and the resulting oxynitrides from ammonolysis at different temperatures (400, 600, 700 and 900 °C) for 6h..

Figure 4 Rietveld patterns of the X-ray powder diffraction data of the sample obtained upon ammonolysis of the $SrMoO_4$ at 600 °C for 4 h. Blue tick marks are Bragg peak positions of related phase as $SrMoO_{3.61(3)}N_{0.39(3)}$ (the ratio of O/N was fixed based on the results of the elemental analysis). The green line at the bottom denotes the difference intensities between the observed and calculated profiles. Table S3 summarizes the results of the structure refinement.

Yang et. al. [36] reported the formation of analogous scheelite-type $EuWO_{4-y}N_y$ oxynitride as intermediate phase during the nitridation from $Eu_2W_2O_9$ to $EuWO_{1+x}N_{2-x}$. However, in their case, the nitrogen substitution is compensated by the partial oxidation of Eu^{2+} to Eu^{3+} (y=0.04 in $EuWO_{4-y}N_y$; i.e., $Eu^{2+}_{1-y}Eu^{3+}_{y}WO_{4-y}N_y$, [36, 37]). In our system, Sr^{2+} is not able to be oxidized to Sr^{3+}, so a different mechanism must be responsible for the formation of the nitrogen-containing scheelite-based phase. A likely explanation is that the generation of oxygen vacancies compensates the extra negative charge due to the replacement of oxygen by nitrogen within the pre-formed crystallites, as usually occurs for nitrogen-doped TiO_2 [38, 39] or HfO_2 [40]. As shown in HRTEM within FFT pattern (Figure 5), the crystalline phase in the sample obtained after ammonolysis of $SrMoO_4$ at 600 °C for 4h was indexed as tetragonal (*I 41/a*, i.e., same as scheelite-type $SrMoO_4$) and exhibited the presence of pores. Some defect regions with different fringe distance were observed as well probably due to the distortion of lattice. Interestingly, thermogravimetric analysis of the $SrMoO_4$ in ammonia revealed a slight mass increase of the sample at temperatures up to 600 °C (Figure 6), indicating that the oxygen, which is expected to be released from $SrMoO_4$ upon ammonolysis, might be stored at intermediate temperature in the pores or interstitially in the structure as molecular oxygen[13] before being released (as shown by mass loss of $SrMoO_4$ at temperatures beyond 700 °C, see Figure 6). This was shown to be the reason for anomalous magnetic behavior at *T*= -219 ^{0}C (54 K) as reported by Longvinovich et. al..[13] The sharp weight loss above 650 ^{0}C is attributed to the complete conversion from scheelite to perovksite resulting in 1 mol oxygen released. Elemental analyses confirm the expected oxygen loss for samples heated in NH_3 between 600 and 700 ^{0}C and are in agreement with the measured mass loss, indicating that nitrogen is already incorporated in the sample at 600 ^{0}C. (Table 1 and Table S6)

Based on all these observations, we conclude that the nitridation of $SrMoO_4$ occurs prior to the reduction of W^{6+} during ammonolysis, thus scheelite-type $SrMoO_{4-x}N_x$ forms as an intermediate phase and decomposes fast according to the following paths (σ stands for amount of oxygen vacancies):

$$SrMoO_4 + xNH_3 \xrightarrow{\sim 600\,^{\circ}C} SrMoO_{4-\sigma-x}V_{O\,\sigma}^{\cdot\cdot}N_x + (\frac{\sigma}{2})O_2 + xH_2O + \frac{x}{2}H_2 \quad [6]$$

$$SrMoO_{4-\sigma-x}V_{O\,\sigma}^{\cdot\cdot}N_x + NH_3 \xrightarrow{>600\,^{\circ}C} SrMoO_{3-x-y}N_{x+y} + H_2O + H_2 \quad [7]$$

Figure 5 HRTEM micrographs of $SrMoO_4$ after heating at 600 ^{0}C for 4 h.

Table 1 Experimental and calculated mass loss of $SrMoO_4$ upon ammonolysis at 600 and 700 °C. The calculated mass loss relies on the evolution of the chemical composition of the sample upon ammonolysis.

Specimens	Experiment	Empirical Formula	Calculated
$SrMoO_4$_NH600_4H	0.4218 g	$SrMoO_{3.61}N_{0.39}$	
$SrMoO_4$_NH700_12H	0.3925 g	$SrMoO_{1.96}N_{1.04}$	
Mass loss (wt %)	6.95		6.97

Figure 6 TG curve of $SrMoO_4$ under ammonia atmosphere from room temperature to 800 ^{0}C.

3.3 Ammonolysis of $SrMoO_4$ vs. $SrMoO_3$

In order to investigate the influence of the oxide precursor on the final oxynitride, we converted the scheelite-type $SrMoO_4$ into $SrMo(O,N)_3$ via a two-step process as well. In a first step, the scheelite-type oxide $SrMoO_4$ was easily reduced to the perovskite-type $SrMoO_3$ (Figure S7) upon thermal annealing at 900 °C for 6 h under forming gas (mixture of 5 vol% H_2 and 95 vol% N_2). In a subsequent step, $SrMoO_3$ underwent ammonolysis at 700 °C for 4 h (same conditions as for $SrMoO_4$) to achieve $SrMo(O,N)_3$. Interestingly, the nitrogen content of the phase-pure perovskite-type oxynitride (empirical formula $SrMoO_{2.77(3)}N_{0.23(3)}$, see the Rietveld refinement data of the neutron diffraction pattern shown in Figure 7a) obtained from perovskite-type $SrMoO_3$ was significantly lower than that of the oxynitride obtained under the same conditions from $SrMoO_4$ ($SrMoO_{2.19(2)}O_{0.81(2)}$). This obviously relates to the oxidation state of Mo in $SrMoO_4$ and $SrMoO_3$ and its evolution in ammonia atmosphere which will be discussed later.

Moreover, the attempt to prepare perovskite-type $SrWO_3$ upon reducing $SrWO_4$ at high temperatures was unsuccessful.

Figure 7 Rietveld patterns of the neutron powder diffraction data of the sample obtained upon ammonolysis of the (a) $SrMoO_3$ at 700 °C for 4 h (FIREPOD, E9); (b) $SrMoO_4$ at 700 °C for 4 h (HRPT, SINQ) and (c) $SrWO_4$ at 900 °C for 4 h (FIREPOD, E9). Blue tick marks are Bragg peak positions of related phase as (a) $SrMoO_{2.77(3)}N_{0.23(3)}$; (b) $SrMoO_{2.19(2)}N_{0.81(2)}$ and (c) $SrWO_{1.50(6)}N_{1.50(6)}$. Green line at the bottom denotes the difference intensities between the observed and calculated profiles.

3.4 Structure verification of perovskite oxynitrides

The neutron powder diffraction data measured at room temperature for $SrMo(O,N)_3$ and $SrW(O,N)_3$ were refined by the Rietveld method on the basis of the cubic *Pm-3m* perovskite-type structure (Figure 7, Table 2). The refined O/N content of $SrMoO_{2.19(2)}N_{0.81(2)}$ (700 °C for 4 h) and $SrWO_{1.50(6)}N_{1.50(6)}$ (900 °C for 4 h) are consistent with the results of elemental analysis (Supporting Information, see Table S6).

Table 2 Crystal structure data of $AB(O,N)_3$ perovskite oxynitride

Specimens and parameters		$SrMoO_{2.77(3)}N_{0.23(3)}$	$SrMoO_{2.19(2)}N_{0.81(2)}$	$SrWO_{1.50(6)}N_{1.50(6)}$
S.G.		Pm-3m, Nr. 221	Pm-3m, Nr. 221	Pm-3m, Nr. 221
Z		1	1	1
a,b,c, Å		3.9744(3)	3.9756(1)	3.9856(2)
Sr	x,y,z	0.5, 0.5, 0.5	0.5, 0.5, 0.5	0.5,0.5, 0.5
	B_{iso}, Å^2	0.666(25)	0.879(21)	0.738(56)
	Occ.	1	1	1
Mo/W	x,y,z	0.0, 0.0, 0.0	0.0, 0.0, 0.0	0.0, 0.0, 0.0
	B_{iso}, Å^2	0.298(23)	0.693(18)	0.880(57)
	Occ.	1	1	1
O/N	x,y,z	0.5, 0.0, 0.0	0.5, 0.0, 0.0	0.5, 0.0, 0.0
	B_{iso}, Å^2	0.748(18)	0.799(12)	0.798(32)
	Occ.	2.77(3) /0.23(3)	2.19 (2) /0.81(2)	1.50(6) /1.50(6)

The enthalpies of dissolution (ΔH_{ds}) and formation (ΔH_f) of scheelite-type $SrMoO_4$ and $SrWO_4$ and the corresponding perovskite-type oxynitride samples measured by high temperature oxide melt solution calorimetry are listed in Table 3.

Table 3 Thermochemical data obtained from drop-solution calorimetry of scheelite-type the oxides and their corresponding perovskite-type oxynitrides.

Composition	Crystal structure	ΔH_{ds} (kJ/mol)	ΔH_f(kJ/mol)	ΔH_f(kJ/g-atom)
$SrMoO_4$	Tetragonal/ Scheelite	161.8 ± 1.5	-1561.3 ± 3.1	-260.2 ± 0.5
$SrMoO_{1.96}N_{1.04}$	Cubic/ Perovskite	-291.9 ± 2.3	-1119.1 ± 3.6	-223.8 ± 0.7
$SrWO_4$	Tetragonal/ Scheelite	-162.8 ± 1.5	-1641.2 ± 3.1	-273.4 ± 0.5
$SrWO_{1.5}N_{1.5}$	Cubic/ Perovskite	-537.2 ± 1.9	-952.9 ± 3.6	-190.4 ± 0.7

The enthalpies of formation of the oxides and oxynitrides from the elements were calculated through the thermodynamic cycles shown in Tables S 7 and S 8 and are given in Table 3. The enthalpy of formation of $SrMoO_4$ (-260.2 ± 0.5 kJ/g-atom) is ~ 36 kJ/g-atom more exothermic than that of $SrMoO_{1.96}N_{1.04}$ (-223.8 ± 0.7 kJ/g-atom). Likewise, the enthalpy of formation of $SrWO_4$ (-273.4 ± 0.5 kJ/g-atom) is ~ 83 kJ/g-atom more exothermic than that of $SrWO_{1.5}N_{1.5}$ (-190.4 ± 0.7 kJ/g-atom). Thus, perovskite-type oxynitrides show less favorable enthalpies of formation than their corresponding scheelite-type oxides. Furthermore, the difference of the enthalpy of formation for Sr-W is larger than that of Sr-Mo. This suggests that forming the Sr-W oxynitride is

less favorable and requires higher temperature (as observed), probably for both thermodynamic and kinetic reasons.

In order to attain further insights related to the energetics of the conversion of $SrMO_4$ into $SrM(O,N)_3$ (M=Mo, W) in ammonia atmosphere, the Gibbs free energy (ΔG) of the reaction (8) and (9) was calculated (Table S9 and S10). Since the entropies of $SrMoO_2N$ and $SrWO_{1.5}N_{1.5}$ are not available, we estimated them as 5/6 of the entropy of corresponding scheelite-type oxide. Equation (9) and (11) describe the temperature evolution of the Gibbs free energy of the reaction of $SrMO_4$ with NH_3 to deliver $SrM(O,N)_3$, indicating that the reaction is spontaneous at temperatures exceeding 992 K (i.e., 719. ^{0}C) for $SrWO_4$; whereas for $SrMoO_4$ the reaction seems to be thermodynamically favorable at any of the temperatures used for its ammonolysis (Figure 8). It is worth to point out that only a thermodynamic consideration might not be enough to describe the ammonolysis processes of the scheelite oxides. The kinetics (e.g., activation energy) of the ammonolysis probably play also an important role and thus might explain why the conversion of $SrMoO_4$ to the perovskite oxynitride needs temperatures exceeding 600 ^{0}C and proceeds through an intermediate phase.

$$SrMoO_4 + 2NH_3 = SrMoO_2N + 2H_2O + H_2 + \frac{1}{2}N_2 \quad [8]$$

$$\Delta G_{Sr-Mo}(kJ/mol) = 50.404 - 0.197T \quad [9]$$

$$SrWO_4 + 2NH_3 = SrWO_{1.5}N_{1.5} + \frac{5}{2}H_2O + \frac{1}{2}H_2 + \frac{1}{4}N_2 \quad [10]$$

$$\Delta G_{Sr-W}(kJ/mol) = 175.615 - 0.177T \quad [11]$$

The negative temperature dependence of the free energy reflects a positive entropy of reaction because 1.5 moles of gas are produced.

Figure 8 Gibbs free energy (ΔG) for the ammonolysis of $SrMoO_4$ and $SrWO_4$ (Eqs. (8) and (10), respectively) as function of the temperature.

3.5 Factors affecting the formation of perovskite-type oxynitrides

As addressed above, the experimental results related to the conversion of $BaMoO_4$, $BaWO_4$, $SrMoO_4$ and $SrWO_4$ into perovskite-type oxynitrides are consistent with our prediction[9]. However, $CaMoO_4$ and $CaWO_4$ appear to not be converted to oxynitrides.

Scheelite-type ABO_4 oxides are rather common precursors for the synthesis of perovskite oxynitrides, e.g. $Nd^{3+}V^{4+}O_2N$[41], $Eu^{2+}Nb^{5+}O_2N$[5], $La^{3+}Nb^{4+}O_2N$[42], $Ca^{2+}{}_xSr^{2+}{}_{1-x}W^{5+}O_2N$[43] and so on. The formation of hydrogen due to the dissociation of ammonia under high temperature is beneficial for the reduction of the B-site cation in scheelite-type oxide (e.g. from $A^{2+}B^{6+}O_4$ to $A^{2+}B^{5+}O_2N$ or from $A^{3+}B^{5+}O_4$ to $A^{3+}B^{4+}O_2N$). In the case of using perovskite oxides as precursors for perovskite-type oxynitrides, the B-site cation has to be oxidized in order to compensate the increasing of the negative charge resulted from nitrogen incorporation (e.g. from $Sr^{2+}Mo^{4+}O_3$ to $Sr^{2+}Mo^{5+}O_2N$). Thus, it seems that scheelite-type oxide precursors are more favorable for the synthesis of perovskite-type oxynitrides.

Moreover, parameters such as the tolerance factor (describing the distortion of the cubic perovskite structure) were shown to be crucial for the formability of perovskite-type oxynitrides.[9] As defined by Goldschmidt,[44] the tolerance factor (t) in ABX_3 is expressed as:

$$t_O = \frac{(r_A - r_X)}{\sqrt{2}(r_B - r_X)} \quad [10]$$

r_A, r_B and r_X being the ionic radii of the A, B and X atoms, respectively.

In our previous work [9], the formability of perovskite-type oxynitrides was also rationalized upon assessing the values of the tolerance factor, defined as in Eq. [11] (see Table 4, as for O/N ratio 2; i.e., ABO_2N):

$$t_{oxy} = \frac{[(r_A + r_O)^8 \times (r_A + r_N)^4]^{1/12}}{\sqrt{2}[(r_B + r_O)^4 \times (r_B + r_N)^2]^{1/6}} \quad [11]$$

Table 4 The tolerance factors for ABO_3 and ABO_2N calculated with the Equations [11] and [12], respectively.

Oxide	**$BaMoO_3$**	**$BaWO_3$**	**$SrMoO_3$**	**$SrWO_3$**	**$CaMoO_3$**	**$CaWO_3$**
t_O	1.03	1.027	0.98	0.975	0.945	0.941
t_{oxy}	1.053	1.048	0.995	0.989	0.959	0.955
Oxynitride	**$BaMoO_2N$**	**$BaWO_2N$**	**$SrMoO_2N$**	**$SrWO_2N$**	**$CaMoO_2N$**	**$CaWO_2N$**
Predicted [#, 9]	N	N	P	P	P	P
Experiment [*]	N	N	P	P	P[11]	N

P: perovskite; N: non-perovskite

[#]: predicted formability of oxynitrides

[*]: formability of oxynitrides for this work

For a general consideration of the formability of perovskite-type oxynitrides, we compare their tolerance factors with those of the

corresponding perovskite-type oxides. The values of the tolerance factors t_o and t_{oxy} calculated from the ionic radii[45] are shown in Table 4 and indicate that the formal substitution of O^{2-} with N^{3-} in $SrMoO_3$, $SrWO_3$, $CaMoO_3$ and $CaWO_3$ reduces the structural distortion (i.e., the tolerance factor become closer to unity), which suggests that the formation of the corresponding perovskite-type oxynitrides is favorable. This is in agreement with the experiment for Sr-Mo/Sr-W compounds and does not fit the experimental observations for Ca-Mo/Ca-W compositions. Large basic cations like Ca typically stabilize higher oxidation states of the transition metals (Mo, W as in our case), [46, 47] thus this may explain why the Ca scheelite-type oxides cannot be converted into oxynitrides.

On the contrary, incorporation of nitrogen within $BaMoO_3$ and $BaWO_3$ increases the structural distortion; thus, the formation of $BaMoO_2N$ and $BaWO_2N$ would be less favorable. This is in agreement with our synthetic observation.

Moreover, the higher covalent character of the B-site-N bond than that of the B-site-O bond might also induce structural distortion into the perovskite structure of oxynitrides as compared to their analogous perovskite oxides, i.e. $B(O,N)_6$ octahedra are expected to be more distorted than their analogous BO_6 octahedra. This structural distortion might be quite pronounced, as for compounds which exhibit so-called secon-order Jahn-Teller distortion [48] (i.e. d^0 B-site octahedra such as in $LaZrO_2N$, $NdTiO_2N$ or $LaTiO_2N$). [4] However, we consider in our compounds $SrM(O,N)_3$ the first-order Jahn-Teller effect being relevant and thus the contribution of the B-site-N covalency on the distortion might not be significant.

4 CONCLUSIONS

In the present study, preparative possibilities to access perovskite-type oxynitrides $AM(O,N)_3$ (A=Ba, Sr, Ca; B=Mo, W) phases upon thermal ammonolysis of scheelite-type AMO_4 oxide precursors were investigated. The as-synthesized results of perovskite-oxynitrides are consistent with our previous prediction in general.

The experimental data reveal that both scheelite-type $SrMoO_4$ and $SrWO_4$ transform into a scheelite-type oxynitride intermediate phase, $SrMO_{4-x}N_x$ (M=Mo, W), which subsequently converts fast into perovskite-type $SrM(O,N)_3$ at temperatures above 600 °C and are in agreement with the high temperature oxide melt solution calorimetry experiments which indicate that the conversion of scheelite $SrMO_4$ into perovskite $SrM(O,N)_3$ is thermodynamically favorable at the used ammonolysis temperatures.

Furthermore, the formability of the perovskite-type oxynitrides depends on the structure of the used oxide precursor (scheelite seems to be favorable, except for large basic A cations) and on the structural distortion described by the tolerance factor.

ACKNOWLEDGMENT

The authors acknowledge Dr. Samuel Bernard (IEM, University Montpellier 2) for the TGA of $SrMoO_4$ in ammonia atmosphere. This work was supported by Dr. Denis Sheptyakov and based on experiments performed at the Swiss spallation neutron source SINQ, Paul Scherrer Institute, Villigen, Switzerland.

Notes and references

[a]. *Fachbereich Material- und Geowissenschaften Technische Universität Darmstadt, 64287 Darmstadt (Germany), Fax: +49 (0) 6151 16 6346 , Tel: +49 (0) 6151 16 6342, E-mail: ionescu@materials.tu-darmstadt.de*

[b.] *Department of Materials and Environmental Chemistry, Arrhenius Laboratory, Stockholm University, S-106 91 Stockholm, Sweden*

[c] *Fachgebiet Keramische Werkstoffe, Institut für Werkstoffwissenschaften und –technologien Fakultät III Prozesswissenschaften, Technische Universität Berlin, Hardenbergstraße 40, 10623 Berlin*

[d.] *Peter A. Rock Thermochemistry Laboratory and NEATORU, University of California Davis, Davis, CA 95616-8779, USA*

[e.] *Helmholtz-Zentrum Berlin für Materialien und Energie, Department of Crystallography, Hahn-Meitner-Platz 1, 14109 Berlin, Germany*

† Electronic Supplementary Information (ESI) available: XRD, FTIR, lattice parameters and phases composition obtained by Rietveld refinement, elemental analysis and the enthalpies of formation results as well as Gibbs free energy calculation. See DOI: 10.1039/b000000x/

‡ This research has been funded by the European Union Seventh Framework Programme (FP7/2007-2013) under the grant agreement FUNEA - Functional Nitrides for Energy Applications. The calorimetry at UC Davis was supported by the U.S. Dept. of Energy, Office of Basic Energy Sciences, grant DE-FG02-03ER46053

1. A. Fuertes, *J Mater Chem*, 2012, 22, 3293-3299.
2. Y. I. Kim and P. M. Woodward, *J Solid State Chem*, 2007, 180, 3224-3233.
3. S. G. Ebbinghaus, H. P. Abicht, R. Dronskowski, T. Müller, A. Reller and A. Weidenkaff, *Prog. Solid State Chem.*, 2009, 37, 173-205.
4. S. J. Clarke, B. P. Guinot, C. W. Michie, M. J. C. Calmont and M. J. Rosseinsky, *Chem Mater*, 2002, 14, 288-294.

5. A. B. Jorge, J. Oro´-Sole´, A. M. Bea, N. Mufti, T. T. M. Palstra, J. A. Rodgers, J. P. Attfield and A. Fuertes, *J Am Chem Soc*, 2008, 130, 12572-12573.
6. D. Logvinovich, R. Aguiar, R. Robert, M. Trottmann, S. G. Ebbinghaus, A. Reller and A. Weidenkaff, *J Solid State Chem*, 2007, 180, 2649-2654.
7. P. Maillard, F. Tessier, E. Orhan, F. Chevire and R. Marchand, *Chem Mater*, 2005, 17, 152-156.
8. F. Chevire, F. Tessier and R. Marchand, *Mater Res Bull*, 2004, 39, 1091-1101.
9. W. J. Li, E. Ionescu, R. Riedel and A. Gurlo, *J Mater Chem A*, 2013, 1, 12239-12245.
10. Y. I. Kim, P. M. Woodward, K. Z. Baba-Kishi and C. W. Tai, *Chem Mater*, 2004, 16, 1267-1276.
11. D. Logvinovich, M. H. Aguirre, J. Hejtmanek, R. Aguiar, S. G. Ebbinghaus, A. Reller and A. Weidenkaff, *J. Solid State Chem.*, 2008, 181, 2243-2249.
12. G. Liu, X. H. Zhao and H. A. Eick, *J Alloy Compd*, 1992, 187, 145-156.
13. D. Logvinovich, J. Hejtmanek, K. Knizek, M. Marysko, N. Homazava, P. Tomes, R. Aguiar, S. G. Ebbinghaus, A. Reller and A. Weidenkaff, *J Appl Phys*, 2009, 105, 023522.
14. R. M. Po Antoine, Y. Lament, C. Michel and B. Raveau, *Mat. Res. Bull.*, 1988, 23, 953-957.
15. A. Navrotsky, *Phys Chem Miner*, 1977, 2, 89-104.
16. J. M. McHale, G. R. Kowach, A. Navrotsky and F. J. DiSalvo, *Chem-Eur J*, 1996, 2, 1514-1517.
17. A. Navrotsky, *Phys Chem Miner*, 1997, 24, 222-241.
18. A. Navrotsky, *J Alloy Compd*, 2001, 321, 300-306.
19. S. H. Elder, F. J. Disalvo, L. Topor and A. Navrotsky, *Chem Mater*, 1993, 5, 1545-1553.
20. M. R. Ranade, F. Tessier, A. Navrotsky, V. J. Leppert, S. H. Risbud, F. J. DiSalvo and C. M. Balkas, *J Phys Chem B*, 2000, 104, 4060-4063.
21. M. R. Ranade, F. Tessier, A. Navrotsky and R. Marchand, *J Mater Res*, 2001, 16, 2824-2831.
22. J. J. Liang, A. Navrotsky, V. J. Leppert, M. J. Paskowitz, S. H. Risbud, T. Ludwig, H. J. Seifert, F. Aldinger and M. Mitomo, *J Mater Res*, 1999, 14, 4630-4636.
23. F. Tessier and A. Navrotsky, *Chem Mater*, 2000, 12, 148-154.
24. I. Molodetsky, A. Navrotsky, F. DiSalvo and M. Lerch, *J Mater Res*, 2000, 15, 2558-2570.
25. P. Fischer, G. Frey, M. Koch, M. Konnecke, V. Pomjakushin, J. Schefer, R. Thut, N. Schlumpf, R. Burge, U. Greuter, S. Bondt and E. Berruyer, *Physica B*, 2000, 276, 146-147.
26. D. M. Tobbens, N. Stusser, K. Knorr, H. M. Mayer and G. Lampert, *Epdic 7: European Powder Diffraction, Pts 1 and 2*, 2001, 378-3, 288-293.
27. P. Thompson, D. E. Cox and J. B. Hastings, *J Appl Crystallogr*, 1987, 20, 79-83.
28. J. Rodriguezcarvajal, *Physica B*, 1993, 192, 55-69.
29. Z. G. Pinsker, *Acta Crystallogr*, 1957, 10, 775-775.
30. P. S. Herle, M. S. Hegde and G. N. Subbanna, *J. Mater. Chem.*, 1997, 7, 2121-2125.
31. Klechkovskaya V.V., Troitskaya N.V. and P. Z.G., *Sov. Phys. Crystallogr. (Engl. Transl.)* 1965, 10, 28-35.
32. R. Scholder and L. Brixner, *Z Naturforsch Pt B*, 1955, 10, 178-179.
33. L. H. Brixner, *J Inorg Nucl Chem*, 1960, 14, 225-230.
34. M. T. Weller and S. J. Skinner, *Int J Inorg Mater*, 2000, 2, 463-467.
35. A. P. A. Marques, M. T. S. Tanaka, E. Longo, E. R. Leite and I. L. V. Rosa, *J Fluoresc*, 2011, 21, 893-899.
36. M. Yang, J. Oro-Sole, A. Kusmartseva, A. Fuertes and J. P. Attfield, *J. Am. Chem. Soc.*, 2010, 132, 4822-4829.
37. A. Kusmartseva, M. Yang, J. Oró-Solé, A. M. Bea, A. Fuertes and J. P. Attfield, *Appl. Phys. Lett.*, 2009, 95, 02210.
38. J. B. Varley, A. Janotti and C. G. Van de Walle, *Adv Mater*, 2011, 23, 2343-2347.
39. A. K. Rumaiz, J. C. Woicik, E. Cockayne, H. Y. Lin, G. H. Jaffari and S. I. Shah, *Appl Phys Lett*, 2009, 95.
40. M. Yang, J. H. Bae, C. W. Yang, A. Benayad and H. Baik, *J Anal Atom Spectrom*, 2013, 28, 482-487.
41. J. Oró-Solé, L. Clark, W. Bonin, J. P. Attfield and A. Fuertes, *Chem Commun*, 2013, 49, 2430-2432.
42. D. Logvinovich, S. C. Ebbinghaus, A. Reller, I. Marozau, D. Ferri and A. Weidenkaff, *Z. Anorg. Allg. Chem.*, 2010, 636, 905-912.
43. Y. Masatomo, F. Uhi, N. Hiromi, O. Kazuki and R. H. James, *J Phys Chem C*, 2013, 117, 18529-18539.
44. V. M. Goldschmidt, *Skrifer Norske Videnskaps-Akad*, I. Mat. Naturv., Oslo, 1926.
45. R. D. Shannon and C. T. Prewitt, *Acta Crystall B-Stru*, 1969, B 25, 925-946.
46. K. Kamata, T. Nakamura and T. Sata, *Chem Lett*, 1975, 81-86.
47. K. Kamata, T. Nakamura and T. Sata, *Mater Res Bull*, 1975, 10, 373-378.
48. R. G. Pearson, *P Natl Acad Sci USA*, 1975, 72, 2104-2106.

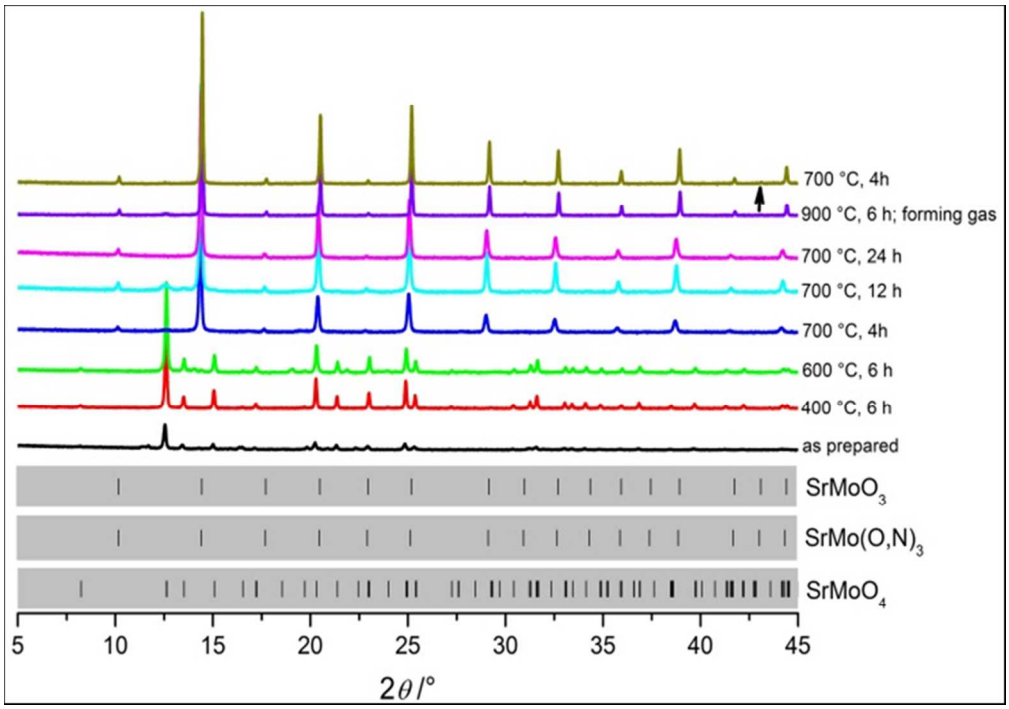

Figure 1 XRD patterns of SrMoO4 after heating at 400, 600 and 700 ^{0}C for different times under an ammonia flow in forming gas (mixture of 5 vol% H2 and 95 vol% N2). Arrow indicates the diffraction pattern of the oxynitride obtained upon ammonolysis of SrMoO3 which was synthesized by reducing SrMoO4 under ammonia flow at 700 ^{0}C.
212x138mm (101 x 108 DPI)

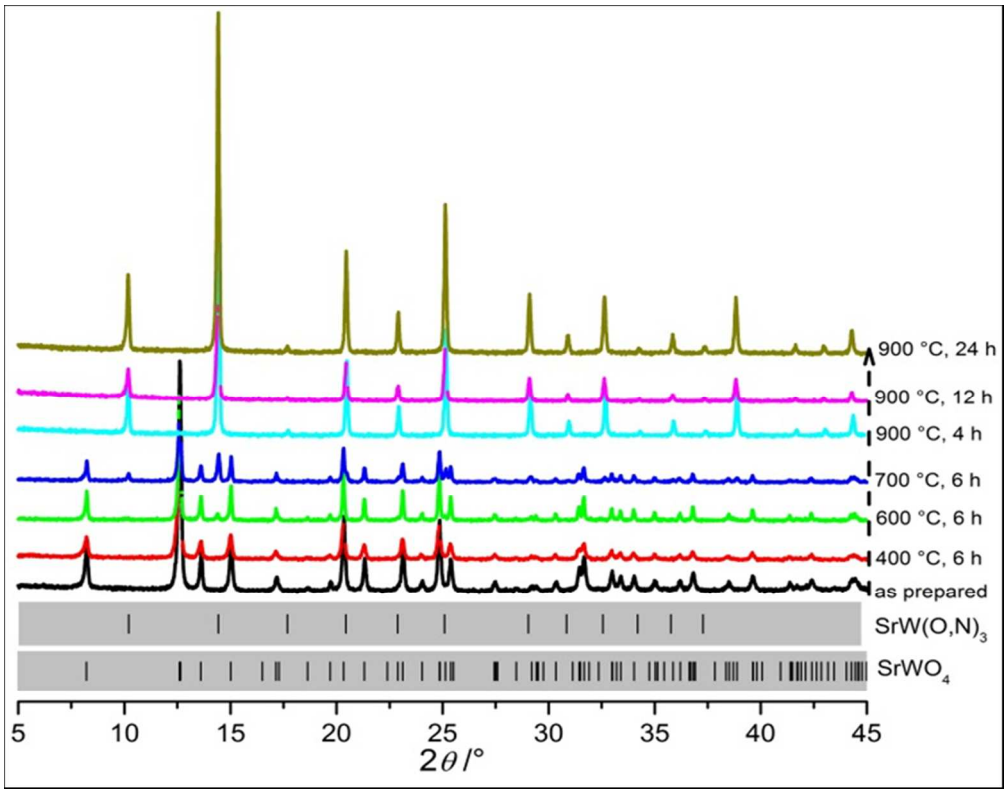

Figure 2 XRD patterns of SrWO4 after heating at 400, 600, 700 and 900 ^{0}C for different time under an ammonia flow.
159x138mm (141 x 127 DPI)

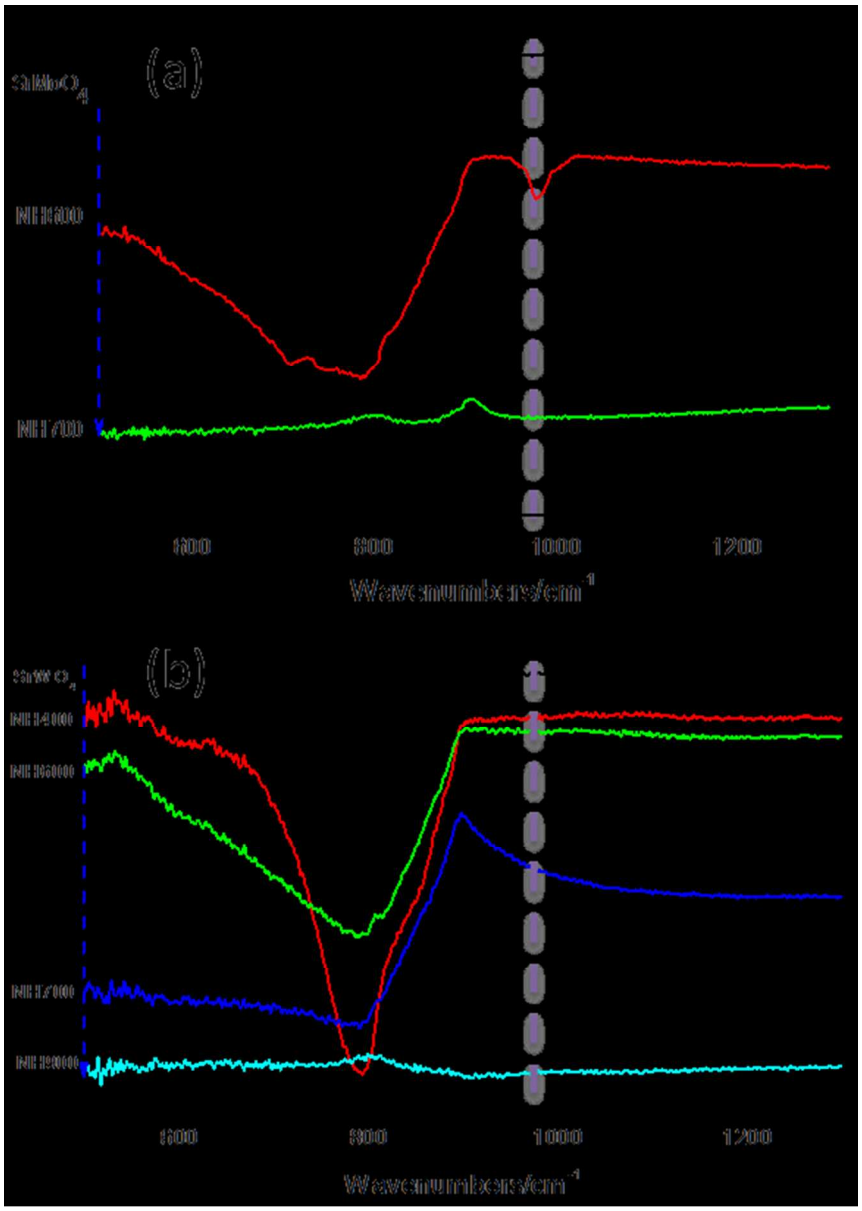

Figure 3 FTIR spectrum of the as-synthesized scheelite oxide (a) SrMoO4, (b) SrWO4 and the resulting oxynitrides from ammonolysis at different temperatures (400, 600, 700 and 900 °C) for 6h..
98x138mm (150 x 150 DPI)

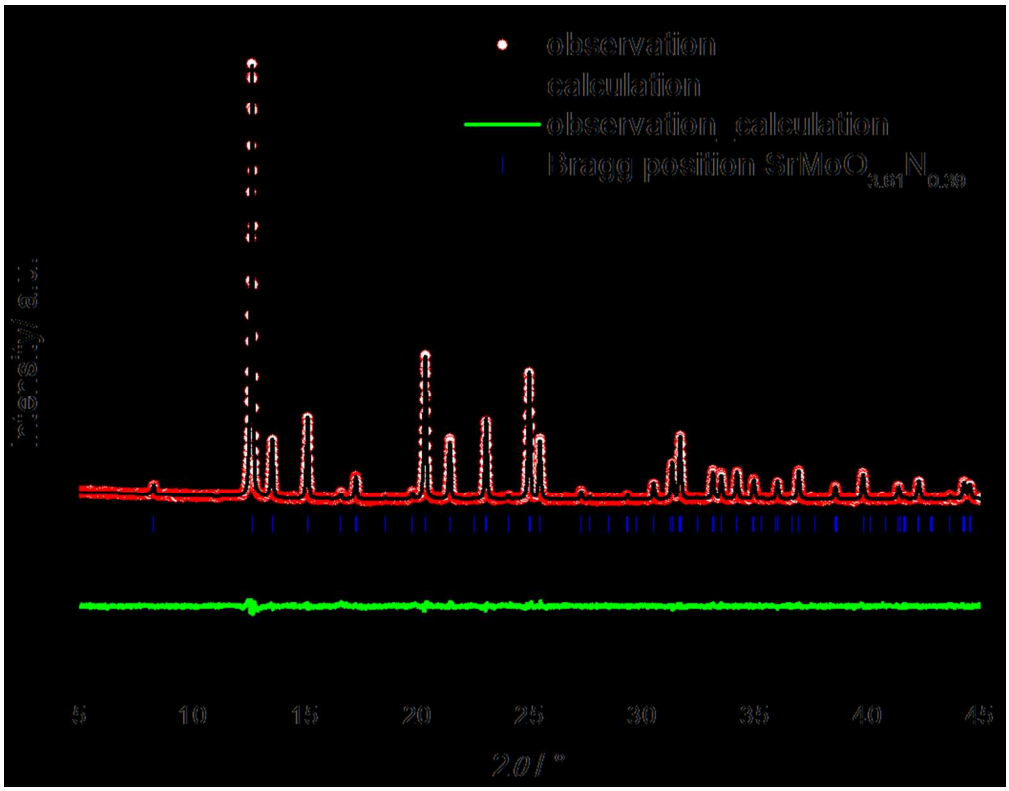

Figure 4 Rietveld patterns of the X-ray powder diffraction data of the sample obtained upon ammonolysis of the SrMoO4 at 600 °C for 4 h. Blue tick marks are Bragg peak positions of related phase as SrMoO3.61(3)N0.39(3) (the ratio of O/N was fixed based on the results of the elemental analysis). The green line at the bottom denotes the difference intensities between the observed and calculated profiles. Table S3 summarizes the results of the structure refinement.
177x138mm (150 x 150 DPI)

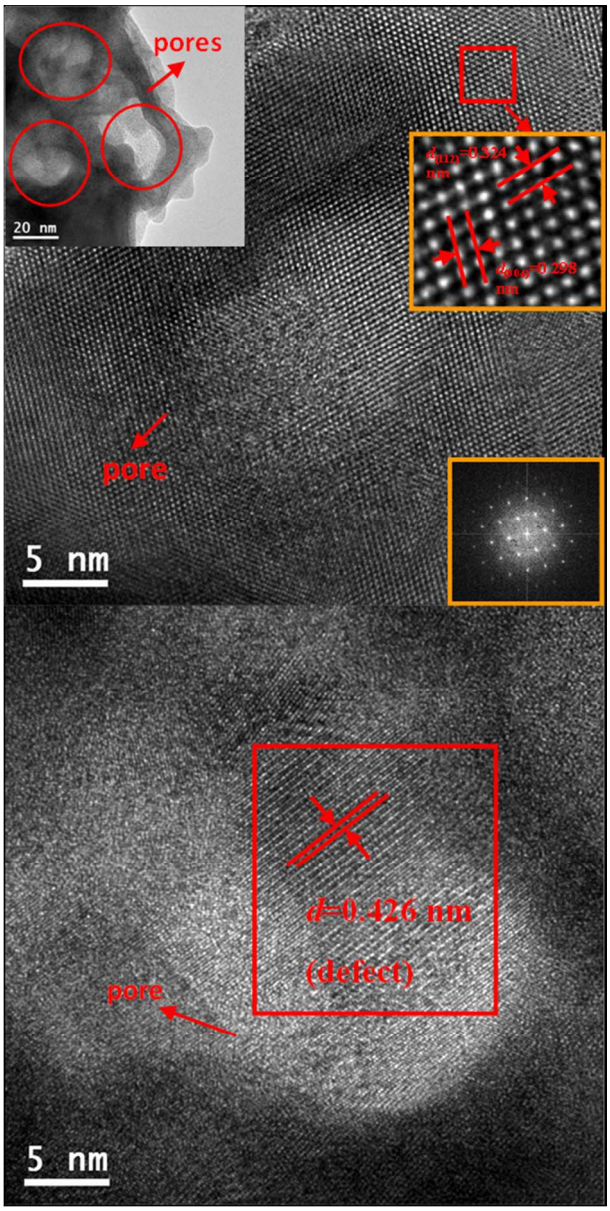

Figure 5 HRTEM micrographs of SrMoO4 after heating at 600 ^{0}C for 4 h.
90x180mm (150 x 150 DPI)

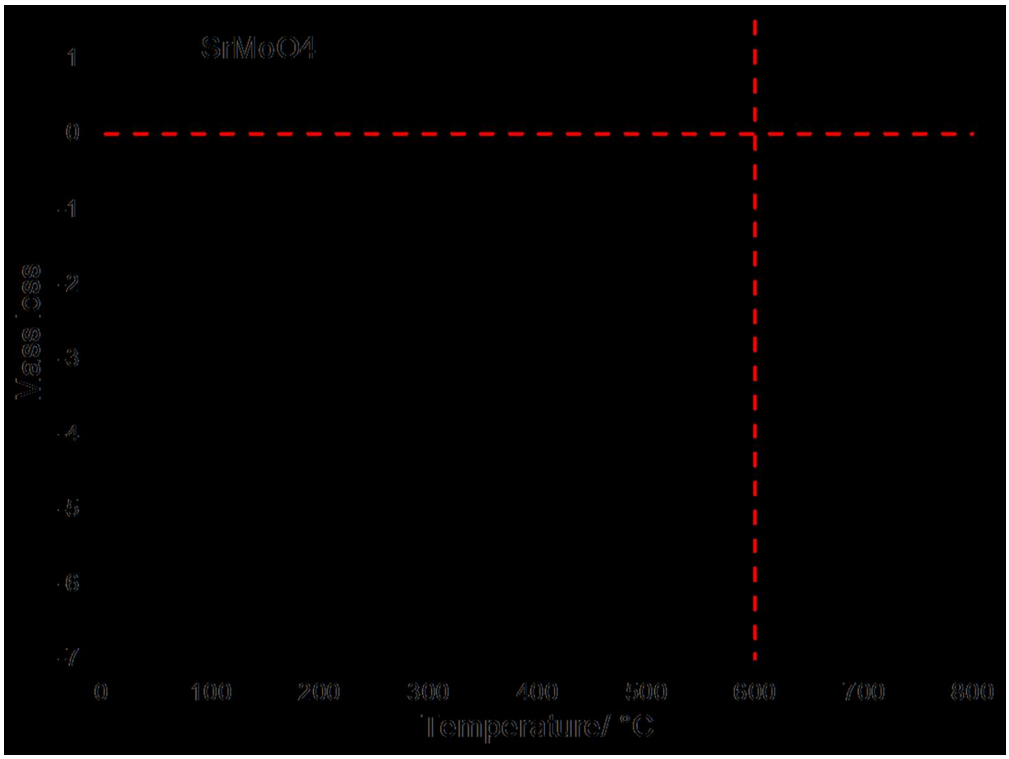

Figure 6 TG curve of SrMoO4 under ammonia atmosphere from room temperature to 800 ^{0}C.
184x138mm (150 x 150 DPI)

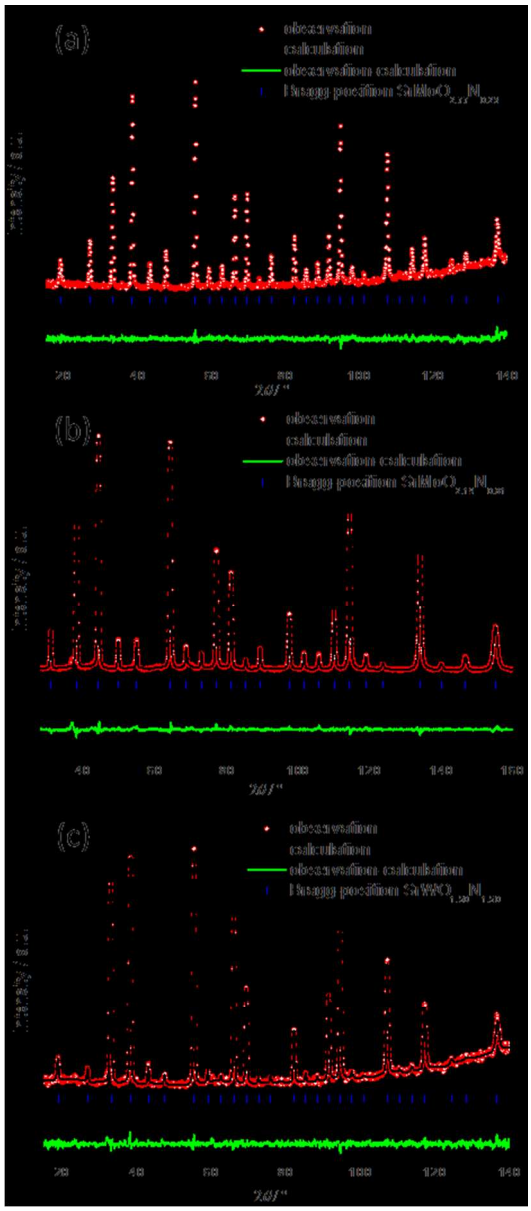

Figure 7 Rietveld patterns of the neutron powder diffraction data of the sample obtained upon ammonolysis of the (a) SrMoO3 at 700 ^{0}C for 4 h (FIREPOD, E9); (b) SrMoO4 at 700 ^{0}C for 4 h (HRPT, SINQ) and (c) SrWO4 at 900 °C for 4 h (FIREPOD, E9). Blue tick marks are Bragg peak positions of related phase as (a) SrMoO2.77(3)N0.23(3); (b) SrMoO2.19(2)N0.81(2) and (c) SrWO1.50(6)N1.50(6). Green line at the bottom denotes the difference intensities between the observed and calculated profiles.
78x180mm (150 x 150 DPI)

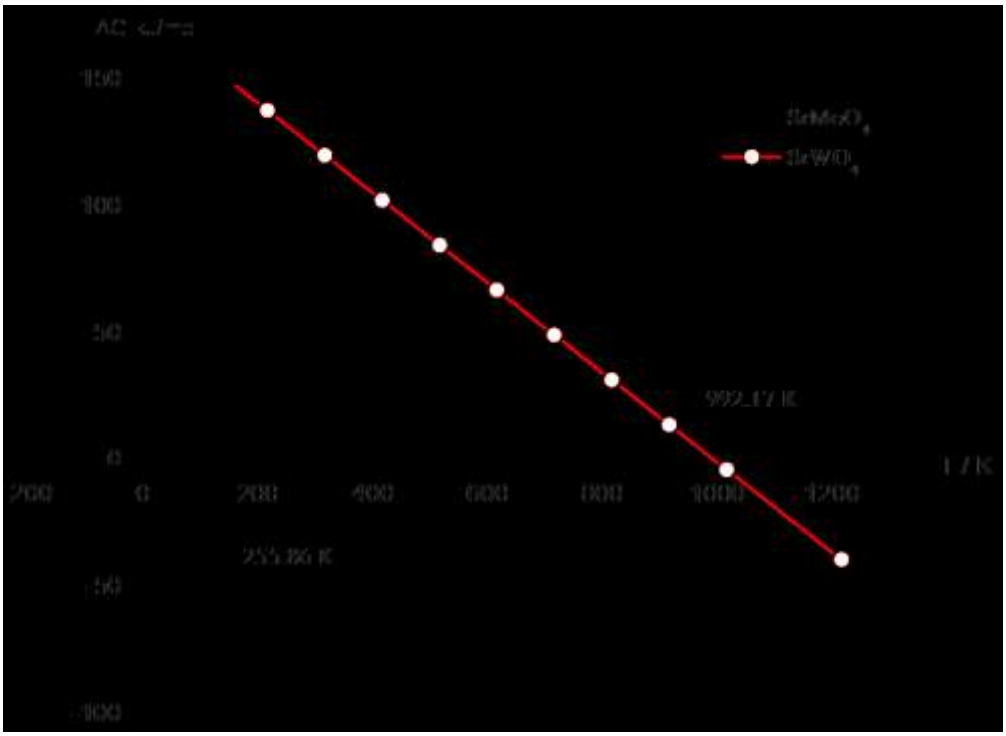

Figure 8 Gibbs free energy (ΔG) for the ammonolysis of SrMoO4 and SrWO4 (Eqs. (8) and (10), respectively) as function of the temperature.
190x138mm (150 x 150 DPI)